Key Points:
- Micromagnetic hysteresis models of magnetite grain shapes obtained by FIB-SEM nanotomography are compared to measured hysteresis loops
- Stress-free models of ~500-nm-long grains yield ~2 times higher M_{rs}/M_s and ~1.5 times higher H_c with microstructures than without
- Comparison to 10 times higher measured bulk M_{rs}/M_s and H_c implies that internal stress from exsolution structures is the dominant effect

Supporting Information:
- Supporting Information S1
- Figure S1

Correspondence to:
G. W. ter Maat,
geertjetermaat@gmail.com

Separating Geometry- From Stress-Induced Remanent Magnetization in Magnetite With Ilmenite Lamellae From the Stardalur Basalts, Iceland

G. W. ter Maat[1] ID, K. Fabian[1] ID, N. S. Church[1] ID, and S. A. McEnroe[1] ID

[1]Department of Geoscience and Petroleum, Norwegian University of Science and Technology, Trondheim, Norway

Abstract Realistic geometries of magnetite grains from the Stardalur volcano, Iceland, were obtained by Focused Ion Beam Scanning Electron Microscopy nanotomography. These magnetite grains are subdivided by oxidation-exsolution lamellae of ilmenite. Magnetic properties of these grains were modeled without internal stress using the three-dimensional micromagnetic code MERRILL. The influence of grain shape and size was isolated by modeling hysteresis loops of the same grains with and without exsolution microstructures. The resulting coercivities H_c are up to 1.5 times higher, and the M_{rs}/M_s ratios are twice as high for the grains with exsolution than for those without. Both modeled values are a factor of 10 smaller than the measured bulk data from the same sample. This difference between stress-free models and measured hysteresis loops suggests that the internal stress due to the formation of the oxidation-exsolution lamellae is the dominant mechanism of coercivity and remanence enhancement. By comparing the approach-to-saturation behavior of modeled and measured hysteresis loops, the internal stress is quantified to about 100 MPa. The formation of lamellae has two effects on magnetic properties. (1) The apparent grain size is geometrically reduced. This effect increases M_{rs} and H_c by up to a factor of 2. (2) The formation of lamellae produces internal stress fields, which provide additional anisotropy energy that deflect the magnetic spins and apparently increase M_{rs} and H_c by up to a factor of 10. Accordingly, stress dominates the remanent magnetic properties in the Stardalur basalts and may be the decisive effect explaining its unusual remanent-dominated ground magnetic anomaly of up to 27,000 nT.

1. Introduction

Understanding the nature and stability of magnetic minerals is of fundamental importance for the interpretation of magnetic anomalies. A remanent magnetization direction close to the inducing field direction can substantially amplify the measured total anomaly. Attribution of such a multicomponent anomaly solely to the induced response, generated predominantly by multidomain magnetite, can lead to a complete misinterpretation of the subsurface geometry, with serious scientific or financial consequences.

Remanent magnetization is commonly oblique to the present field direction, and the vector sum of the remanent and induced magnetizations may differ substantially from the present field direction (Clark, 2014). Modeling of magnetic anomalies is more complicated when the resultant magnetization direction is unknown, and the interpretation of magnetic surveys is highly nonunique if the magnetization is not necessarily parallel to the present field. For example, the dip of a sheet-like body is indeterminate if the direction of magnetization is unknown.

A large positive magnetic anomaly has been measured over the Stardalur volcanic complex, 20 km NE of Reykjavik, Iceland (Friðleifsson & Kristjánsson, 1972). Later, a ground magnetic survey was conducted over the area, yielding a magnetic anomaly of +27 μT above the geomagnetic field intensity of 52 μT (Kristjánsson, 2013). A deep drill core through the center of the anomaly recovered 143 m of olivine tholeiite lavas (Kristjánsson, 2013).

The Stardalur basalts have natural remanent magnetization (NRM) intensities that range from 20 to 120 A/m. In contrast, the average NRM value for Icelandic tertiary lavas is 4 A/m (Kristjánsson, 2002, 2013). The samples yield a mean magnetic susceptibility of 0.07 SI (Stange, 2016; Vahle et al., 2007). The mean Koenigsberger ratio, the ratio between the remanent (M_r) and induced magnetization (M_i; $Q = |M_r|/|M_i|$),

of the Stardalur basalts is Q = 61, demonstrating that the remanent magnetization is an order of magnitude larger than the induced magnetization.

The dominant magnetic carrier in the Stardalur basalts is magnetite, present in volume percent of 1–3%, estimated from saturation magnetization and/or susceptibility (Friðleifsson & Kristjánsson, 1972; Kristjánsson, 2013; Stange, 2016). Minor maghemitization is reported in some of the Stardalur basalt (Helgason et al., 1990; Vahle et al., 2007) but does not explain the exceptional enhancement of magnetization.

The formation of microstructures in magnetite by processes such as oxidation-exsolution, and spinodal decomposition have two major effects on magnetization: (1) change to the shape, size, and composition of the magnetic carriers and (2) these add internal stress fields which strongly distort the magnetic structure. Both effects have implications for stability and strength of remanence, but their relative importance is difficult to assess. The presence of microstructures can change the grain size from multidomain (MD) states to pseudo-single domain (PSD) or stable single-domain (SD) states. The PSD state has traditionally been described as the transitional state from SD with uniform magnetization to a MD state with magnetic domains, within which the magnetization is approximately uniform but differs from that of neighboring domains, separated by relatively narrow domain walls.

Early work on the influence of subdivision of mineral phases in the magnetite-ulvöspinel system found that grains containing intergrowths result in coercivity which is up to 5 times higher than the coercivities from homogeneous grains (Evans & Wayman, 1974). Evans et al. (2006) found that magnetostatic interaction is of extreme importance in a system of magnetite-ulvöspinel intergrowths. Muxworthy (2003) shows that magnetostatic interactions result in a decrease in M_{rs}/M_s and H_c between SD grains, and for PSD grains the effect of interactions is more SD-like or MD-like behavior depending on the anisotropy and grain size. Indirect experimental observation of the interaction field can be made by first-order reversal curve (FORC) diagrams (Pike et al., 1999; Roberts et al., 2000).

The shape of the hysteresis loop is another factor to be considered when studying the influence of microstructures on magnetic properties. The approach-to-saturation behavior of magnetic materials provides insight on the internal stress inside a particle, which can be inferred from the reversible magnetization work U_{rev} (Appel, 1987; Fabian, 2006; Hodych, 1990). Large internal stress in a particle increases the anisotropy energy to values substantially higher than the cubic magnetocrystalline anisotropy of magnetite. Dunlop (2002) demonstrates that the state of internal strain or stress has a large influence on the position of PSD data on a Day plot (Day et al., 1977), where unannealed crushed magnetite samples have higher M_{rs}/M_s ratios and lower H_{cr}/H_c than their annealed counterparts.

Recent studies using micromagnetic calculations indicate that small PSD magnetite and single-vortex states can carry an extremely stable and reliable remanence over billions of years (Nagy et al., 2017). Almeida et al. (2014a, 2014b, 2016) observed magnetic flux closure in magnetite using electron holography and interpreted this structure as the vortex state. Single-vortex grains are the simplest PSD states, which occur in all soft magnetic particles when the SD state becomes unstable. In equidimensional magnetite grains vortex states are stable between 80 nm to 1 μm. At larger sizes these grains form either (1) PSD magnetization structures with inhomogeneous structures and no clear domains or (2) MD magnetization structures, with distinct uniformly magnetized regions with domain walls.

Previous studies using micromagnetic calculations commonly model geometries of idealized shapes (Fabian et al., 1996; Fukuma & Dunlop, 2006; Khakhalova et al., 2018; Newell & Merrill, 1999; Yu & Tauxe, 2008; Witt et al., 2005, Williams & Dunlop, 1995). Natural iron oxide geometries are usually more complicated (e.g., Larson et al., 1969; Shaar & Feinberg, 2013). The finite-element micromagnetic software package MERRILL (Micromagnetic Earth-Related Robust Interpreted Language Laboratory; Fabian & Shcherbakov, 2018; Ó'Conbhuí et al., 2018), allows for simulations of arbitrary particle geometries, including those that represent truly observed magnetic carriers in natural rocks. To acquire 3-D morphologies of such true particle geometries, we used nanotomography by Focused Ion Beam Scanning Electron Microscopy (FIB-SEM). Examples of other studies using MERRILL on magnetic oxides include submicron grains of iron (Einsle et al., 2016; Nagy, Williams, Tauxe, & Muxworthy, 2019a; Nagy, Williams, Tauxe, Muxworthy, & Ferreira, 2019b; Nichols et al., 2019; Shah et al., 2018); magnetite (Lascu et al., 2018) and titanomagnetite (Khakhalova et al., 2018; Khakhalova & Moskowitz, 2019).

FIB-SEM-based models are created for magnetite grains with oxidation-exsolution lamellae of ilmenite from the Stardalur lavas in Iceland. These grains form the basis for subsequent micromagnetic models of true
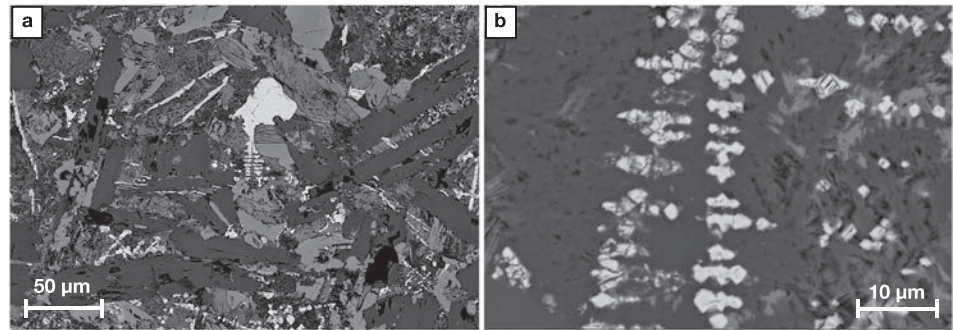
Figure 1. Backscatter scanning electron microscopy images for Sample ST63. (a) Overview BSE image, showing silicates in dark gray and oxides in light gray. The oxides vary in shape; there are large grains as well as abundant smaller grains. The small elongated grains are commonly ilmenite. (b) Dendritic magnetite in light gray with oxidation-exsolution lamellae of ilmenite and exsolution lamellae of spinel. The exsolution lamellae are seen in magnetite of all sizes, even the smallest dendritic grains.

geometries of the oxy-exsolved magnetite grains and are modeled with, and without, exsolution microstructures. Because the micromagnetic simulations include no stress anisotropy, these then isolate the effect of geometric differences on the enhancement of remanence.

By comparing the modeled hysteresis loops with the rock magnetic measurements from the corresponding bulk sample, we provide a method to separate geometric remanence enhancement from stress-induced remanence enhancement. This analysis allows us to approximately quantify the amount of internal stress.

2. Materials and Methods

2.1. Stardalur Basalt Sample

The Stardalur basalts contain abundant magnetite (Figure 1a), with extensive oxidation-exsolution lamellae, and discrete ilmenite grains. Large magnetite grains (>200 μm) contain oxidation-exsolution lamellae of ilmenite and spinodal decomposition of spinel commonly in the form of needles or blades. The smaller dendritic grains (Figure 1b) mainly contain oxidation-exsolution lamellae of ilmenite. The widespread occurrence of oxidation-exsolution lamellae leads us to question whether their presence provides a possible explanation for the unusual strong remanent magnetization and by which physical mechanism these microstructures influence the magnetic properties.

The sample studied in detail is ST63, which has a density of 2.78 g/cm^3, a susceptibility of 0.075 SI, and an NRM of 87.9 A/m (Kristjánsson, 2013; Stange, 2016). A thin section of ST63 with a thickness of 30 μm was used for FIB-SEM nanotomography.

2.2. Petrophysical and Rock Magnetic Properties

Rock magnetic properties were studied using a Princeton instruments Vibrating Sample Magnetometer. Hysteresis loops were measured in a maximum field of 1 T, giving the parameters saturation magnetization (M_s), remanent saturation magnetization (M_{rs}), and coercivity (H_c). FORCs (Pike et al., 1999; Roberts et al., 2000) were measured on a Princeton Instruments Vibrating Sample Magnetometer at NTNU. A FORC diagram is calculated from a set of partial hysteresis loop measurements. The sample is saturated in a saturating field H_{sat}, after which a reversal field H_r is applied and the magnetization is measured during the increase of the field H from H_r to H_{sat}. This is repeated for regularly spaced values of H_r. The FORC distribution is defined as $\rho(H, H_r) = \frac{1}{2}\frac{\delta^2 M}{\delta H_r \delta H}$ (Pike, 2003), where M is the measured magnetization and the unit of the mass normalized FORC distribution is Am^2/kg T^2. Calculation of the FORC distribution used the FORCinel software (Harrison & Feinberg, 2008), with the VARIFORC smoothing algorithm (Egli, 2013). The resulting FORC diagram is a contour plot of (H, H_r), with the axes $H_c = (H - H_r)/2$ and $H_u = (H - H_r)/2$.

To identify and characterize the remanent component, we measured nonlinear Preisach distributions using field steps adapted to the distribution of the coercive fields of the sample (Church et al., 2016). A nonlinear Preisach diagram incorporates aspects of FORC and isothermal remanent magnetization acquisition curves,

which are acquired using logarithmic field steps. A complete Preisach map consists of a series of remanence curves. These curves are obtained by applying, and removing, a large positive saturating field, followed by applying and removing a negative conditioning field $H_a = -H_i$. Subsequently, the positive back fields $H_b = +H_j$ are applied and removed. The resulting remanence for each step is defined by $M_r(-H_i+H_j) = M_r(H_a, H_b)$. The Preisach maps plot the scaled magnetization change, rather than the magnetization density (Church et al., 2016).

2.3. FIB-SEM Nanotomography

FIB-SEM nanotomography is a relatively new technique to obtain the 3-D geometry of micrograins. Here, the nanotomography was performed on a dual beam FEI Helios G4 UX instrument at the Nanolab facility at NTNU using the Auto Slice&View 4 application from FEI. A liquid metal Ga-ion source can be used to mill away parts of the sample, using variable currents (and therefore milling speeds) or to deposit material onto the sample via a gas injection system. Imaging used an accelerating voltage of 15 kV and a beam current of 3.2 nA. The image resolution is $3,072 \times 2,048$, the working distance was 4 mm, and the dwell time was 10 µs.

Figure 2 sketches the sample preparation and imaging steps for slice and view. First, a protective layer of 2-µm platinum is deposited on the region of interest (green in Figure 2a), and a fiducial mark is created to correct for horizontal drift during the process. Then the area around the region of interest is milled away to obtain a 20-µm-deep trench around it. For the slice-by-slice milling a stage tilt of 52° is required to orient the FIB perpendicular to the surface. Slices with thickness of 0.02 µm are stepwise removed with a FIB beam current set to 2.6 nA. After each milling step two images were taken, one by the Everhart-Thornley detector in secondary electron mode and one by the mirror detector for a backscattered electron image.

The resulting images were loaded into the image analysis software FIJI and then aligned using the macro TrakEM. The resulting aligned Tagged Image File Format (TIFF) stack forms the input for the three-dimensional mesh generation.

2.4. Mesh Generation for Micromagnetic Modeling

In order to obtain a 3-D reconstruction of a single grain, the desired grain was segmented out manually from the aligned TIFF stack in FIJI by tracing the edges of the grains from the secondary electron images. The resulting images were then smoothed and loaded into Paraview (Ahrens et al., 2005) to create a stereolithography (STL) file. Paraview is an open source tool, which is commonly used for the visualization of 3-D data.

To define the voxel size of the data we use the "common data spacing" option. The x size of each voxel is obtained from the FIB results. Since the SEM images are obtained at an angle of 52°, the resulting pixel size in the y direction is smaller than the real pixel size in the y direction. The actual pixel size in the y direction is $Y_{real} = Y_{pixel}/\sin(52°)$. The z size of each voxel is defined by the slice thickness from the slice-and-view procedure and is 0.02 µm in this case. In Paraview the smoothed TIFF stack with the correct voxel size is loaded and exported as a STL file.

To create a tetrahedral volume mesh that is needed for MERRILL we use Iso2mesh (Fang & Boas, 2009) in Octave, which are both open source software packages. In Iso2Mesh the STL file can be loaded and transformed into a tetrahedral volume mesh using the cgals2m function. The mesh can be saved into a Patran (MSC-Software) like PATmesh file which is read by MERRILL, using the simple routine merrillsave.m for Octave (available together with the meshes in ter Maat (2019—database).

A node spacing of the generated mesh does not exceed the exchange length of ~9 nm in magnetite, a requirement which is essential to resolve the expected spatial variation of the magnetization within the model geometry Ó'Conbhuí et al., 2018).

Meshes were generated from FIB-SEM nanotomography data for two magnetite grains, G4 (Figure 3) and G5 (supporting information Figure S1). The more complex geometries of meshes G4W and G5W include oxidation-exsolution lamellae. In these, only the region containing magnetite is extracted from the FIB-SEM data. In contrast, the geometries for G4N and G5N are only the outlines of the host magnetite grains and represent the magnetic prior to formation of any microstructure (Figure 3). In Figure 3 the meshes for G4N and G4W are shown, including cross sections of the mesh geometries, where red indicates magnetite in both meshes, and gray indicates ilmenite lamellae in the G4W and magnetite in G4N.
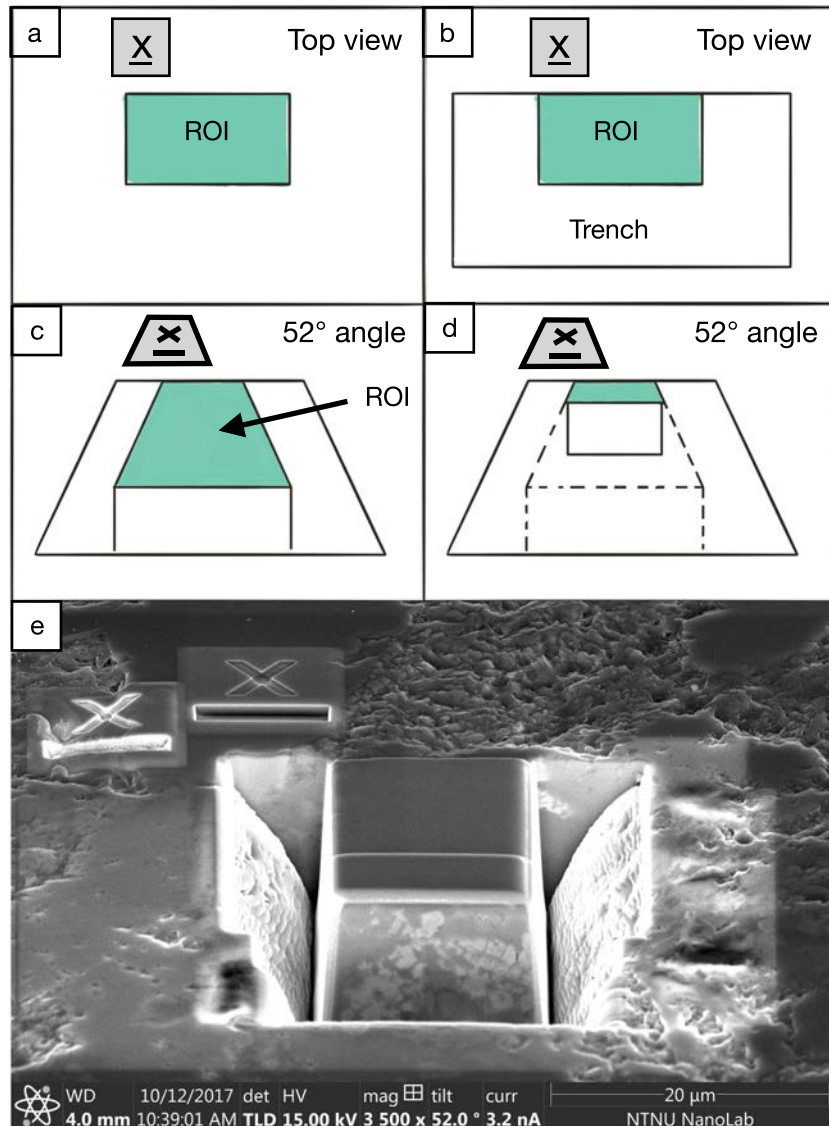
Figure 2. FIB-SEM slice-and-view procedure. (a) A protective layer of platinum (green) is deposited on the region of interest (ROI) and a fiducial mark is created for drift correction. An area around the ROI is selected (b) and milled away. The sample is rotated to an angle of 52° to orient the focused ion beam (FIB) at perpendicular to the surface (c). The FIB mills away material in steps of 20 nm and the SEM images the new surfaces until the entire ROI is milled away and imaged (d). (e) Actual backscatter SEM image taken at 52° angle.

2.5. Micromagnetic Simulations

Micromagnetic simulations were performed using the open-source software MERRILL for 3-D micromagnetics (Fabian & Shcherbakov, 2018; Ó'Conbhuí et al., 2018). MERRILL works by minimizing micromagnetic energies, which are the exchange, magnetostatic, demagnetizing and anisotropy energies. The anisotropy energy tends to align the magnetization with certain crystallographic axes (Kittel, 1949). The cubic anisotropy energy density of magnetite can be expressed by $E_a(m) = K_1\left(m_x^2 m_y^2 + m_y^2 m_z^2 + m_z^2 m_x^2\right)$, where $\mathbf{m} = (m_x, m_y, m_z)$ is the unit vector parallel to the magnetization, if the cubic axes correspond to the coordinate axes (Akulov, 1931). The exchange energy density (Heisenberg, 1928) is represented by a term: $E_{ex} = A[(\nabla m_x)^2 + (\nabla m_y)^2 + (\nabla m_z)^2]$. The material constants for all four models were chosen to correspond to magnetite at room temperature: cubic anisotropy with $K_1 = -13.2658$ kJ/m^3, exchange constant $A = 1.33487 \ 10^{-11}$ J/m, saturation magnetization $M_s = 480.768$ kA/m (Ó'Conbhuí et al., 2018). These
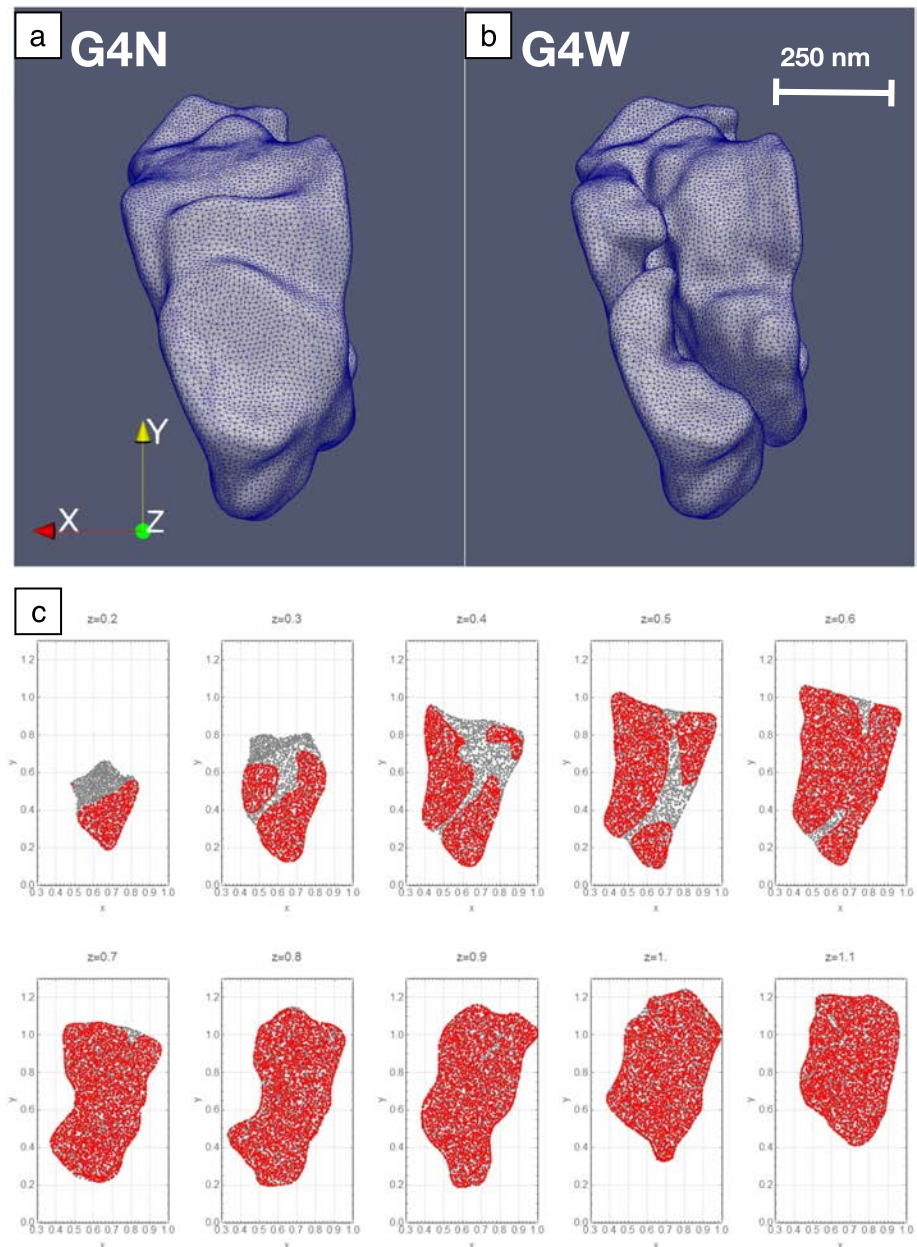
Figure 3. Meshes G4N (a) and G4W (b) which were used the micromagnetic simulations. Mesh G4N is based on the geometry of G4W but fills exsolution microstructures to represent a grain without exsolution. (c) Planar *x-y* cross sections along the *z* direction from the bottom of (a) and (b). In G4W gray areas represent exsolved ilmenite, while in G4N they also contain magnetite

parameters are built into the software. The simulations were performed on the IDUN/EPIC cluster at NTNU and an Apple MacMini with a 3-GHz Intel i7 processor and 16 GB of RAM.

Each particle was initialized at an applied −500mT saturating field, with a random magnetization state that immediately converged to a SD state. Simulations then stepwise minimized the total micromagnetic energy at increasing applied fields in steps of 10 mT, where the final state of the previous field step was used as initial state of the next step. To resolve better the low-field switching behavior for particles G4N and G4W, additional models were created between the states at −10 and 10 mT by using an increment of 1 mT. The combined procedure yields the lower branch of a hysteresis loop. The upper branch was calculated using time-inversion symmetry of the Maxwell equations, which guarantees that it is point symmetric to the

Table 1

External Field Directions and Hysteresis Parameters for Particles G4N (Without Microstructures) and G4W (With Exsolution Microstructures)

External field direction		Alignment with particle long axis					
φ	θ	cos (°)	M_{rs}	M_s	M_{rs}/M_s	H_c (mT)	N
G4N		**Mean**	**0.013**	**0.956**	**0.014**	**1.88**	**0.24**
0.0	90.0	0.7	0.021	0.964	0.021	2.49	0.20
222.5	5.5	0.0	0.006	0.950	0.007	1.02	0.27
85.0	11.0	0.5	0.023	0.971	0.024	2.26	0.16
−52.5	16.6	0.9	0.008	0.957	0.008	1.42	0.31
170.0	22.4	0.6	0.016	0.921	0.018	3.52	0.36
32.5	28.4	0.2	0.010	0.949	0.010	1.26	0.21
218.1	23.9	0.4	0.011	0.958	0.011	1.61	0.25
117.5	41.8	0.8	0.007	0.970	0.007	0.27	0.06
−59.3	32.7	0.9	0.011	0.965	0.011	1.96	0.30
202.5	59.0	1.0	0.019	0.959	0.020	3.02	0.26
G4W		**Mean**	**0.021**	**0.954**	**0.022**	**2.70**	**0.21**
0.0	90.0	0.7	0.006	0.959	0.007	0.78	0.20
222.5	5.5	0.1	0.017	0.947	0.018	2.52	0.24
85.0	11.0	0.5	0.050	0.973	0.051	3.14	0.10
−52.5	16.6	0.9	0.014	0.955	0.014	2.43	0.29
170.0	22.4	0.6	0.015	0.923	0.016	3.13	0.36
32.5	28.4	0.2	0.018	0.952	0.019	1.52	0.14
218.1	23.9	0.4	0.017	0.950	0.018	3.09	0.29
117.5	41.8	0.8	0.038	0.966	0.040	4.43	0.19
−59.3	32.7	0.9	0.020	0.962	0.021	3.49	0.29
202.5	59.0	1.0	0.015	0.953	0.016	2.44	0.26

Note. The alignment of the external field direction with the longest axis of the particle is indicated by the cosine of the angle, which means for cos(°) = 1 the field direction is aligned with the particle longest axis, and for cos(°) = 0 the field direction is perpendicular to the particle longest axis. The saturation remanent (M_{rs}) and saturation magnetization (M_s) are given in terms of the theoretical saturation magnetization used in the model. The value of M_s in the table is the saturation magnetization as inferred from the modeled hysteresis loop and is slightly lower than the real M_s if saturation is not reached by the maximally applied model field. The coercivity (H_c) is given in mT and N is the self-demagnetizing factor.

lower branch. The field was applied in ten different external field directions. The directions are listed in Table 1 and form a Fibonacci lattice over the sphere to ensure that they approximately represent equal areas. By averaging the simulation results over the sphere, a more reliable approximation of the bulk hysteresis behavior is achieved.

3. Results

3.1. Rock Magnetic Properties of Sample ST63

Standard rock magnetic properties of Sample ST63 are compiled in Figure 4. A hysteresis loop of Sample ST63 is shown in Figure 4a with the measured loop in red, and the loop corrected for the high-field slope in blue. The sample has a saturation magnetic moment of $\mu_s = 1.13$ mAm^2, a saturation remanent magnetic moment of $\mu_{rs} = 0.22$ mAm^2, and a coercivity of $H_c = 13.9$ mT. The squareness is $M_{rs}/M_s = 0.17$. The coercivity of remanence was obtained from the backfield curve and has a value of $H_{cr} = 30.1$ mT. Unmixing of the backfield curve indicates the presence of two coercivity components at ~10 and ~44 mT (Figure 4b).

The ratio saturation remanent magnetization (M_{rs}) to saturation magnetization (M_s) is plotted against the ratio coercivity of remanence (H_{cr}) to coercivity (H_c) on a Day plot (Day et al., 1977). The theoretical areas for SD and PSD behavior are from Dunlop (2002). The Sample ST63 plots on the magnetite SD-MD mixing line of Dunlop (2002) within the region of PSD behavior (Figure 4c). It closely resembles the data point for an unannealed crushed natural magnetite of 1-μm size and also lies near a data point for a hydrothermal magnetite of 0.1-μm size (Dunlop, 2002, Figure 8). Micromagnetic modeling can help to decide if either of these options can be used to understand the behavior of the Stardalur magnetite.

The FORC diagram of Sample ST63 (Figure 4d) qualitatively would be described as dominated by a strong PSD signal. The spread along the H_u axis may indicate the presence of MD carriers. In addition, the central ridge along the H_c axis, extending to ~200 mT, indicates the presence of noninteracting high-coercivity SD particles. The asymmetric spread about the central ridge, up to 150 mT, reflects high-coercivity interacting remanence carriers.

The Preisach remanence map (Figure 4e) shows that more than 90% of the coercivity signal is concentrated between 10 and 100 mT. The distribution shows very little signal below 5 mT, indicating that MD magnetite does not substantially contribute to the remanent magnetization. Between 10 and ~70 mT the distribution is widely spread perpendicular to the diagonal, with a maximal spread both above and below the diagonal at ~30 mT. The shape above and below the diagonal is different, with a broader spread below the diagonal and a narrower and longer spread above the diagonal. At coercivity values above 50 mT the spread is less pronounced and offset below the diagonal. The high coercivity component along the diagonal continues well above 100 mT. The spreading along the diagonal represents noninteracting SD particles. There is a negative region below the diagonal around $H_a > 100$ mT and H_b 20–50 mT and above the diagonal at $H_a > 50$ mT and $H_b > 100$ mT.

3.2. Micromagnetic Simulations

Micromagnetic simulations of hysteresis loops with 10 different external field directions for grains G4 and G5 were performed. Modeling results for G4 models are presented here (Figures 5 and 6), and the results for G5 are provided in the supporting information (Figure S2).

In Figures 5a and 5b the remanence states are shown for the grain without exsolution lamellae (G4N) and the grain that does contain exsolution lamellae (G4W), with the applied field in the z direction (see
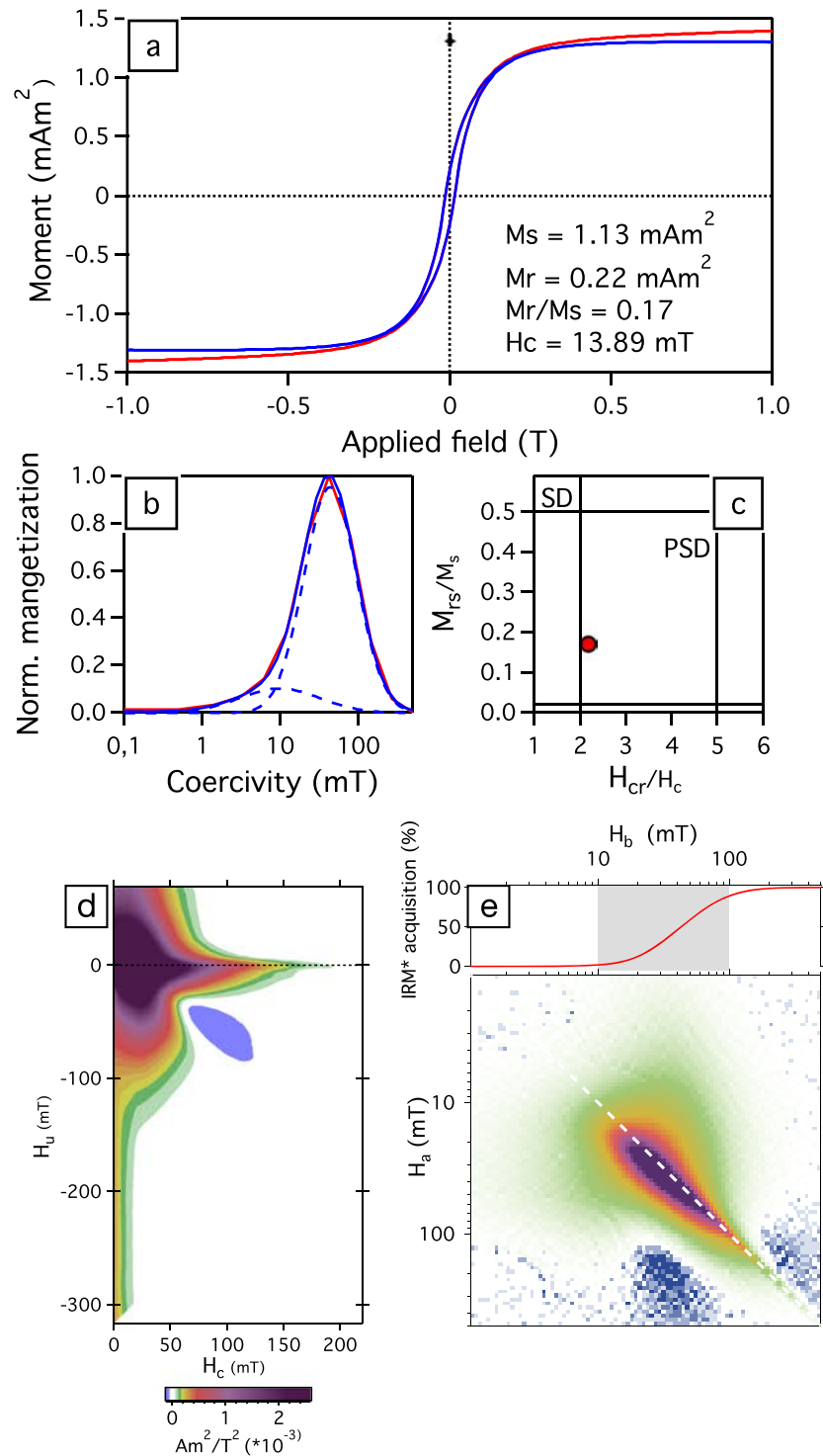
Figure 4. (a) The measured hysteresis loop of Sample ST63 is characterized by a coercivity of 13.9 mT and a squareness ratio (M_{rs}/M_s) of 0.17. (b) IRM unmixing curve. The backfield curve unmixing results in two peaks, at ~10 mT and at ~44 mT. (c) ST63 on a day plot (Day et al., 1977). The regions of SD and PSD behavior are from Dunlop (2002) and the sample plots in the PSD region. (d) The FORC distribution of ST63 is characterized by a strong PSD signal. The central ridge indicates the presence of noninteracting SD carriers. (e) The nonlinear Preisach map shows the presence of a SD component, the dominant signal appears to originate from PSD magnetite. A substantial remanence contribution from MD magnetite is invisible.
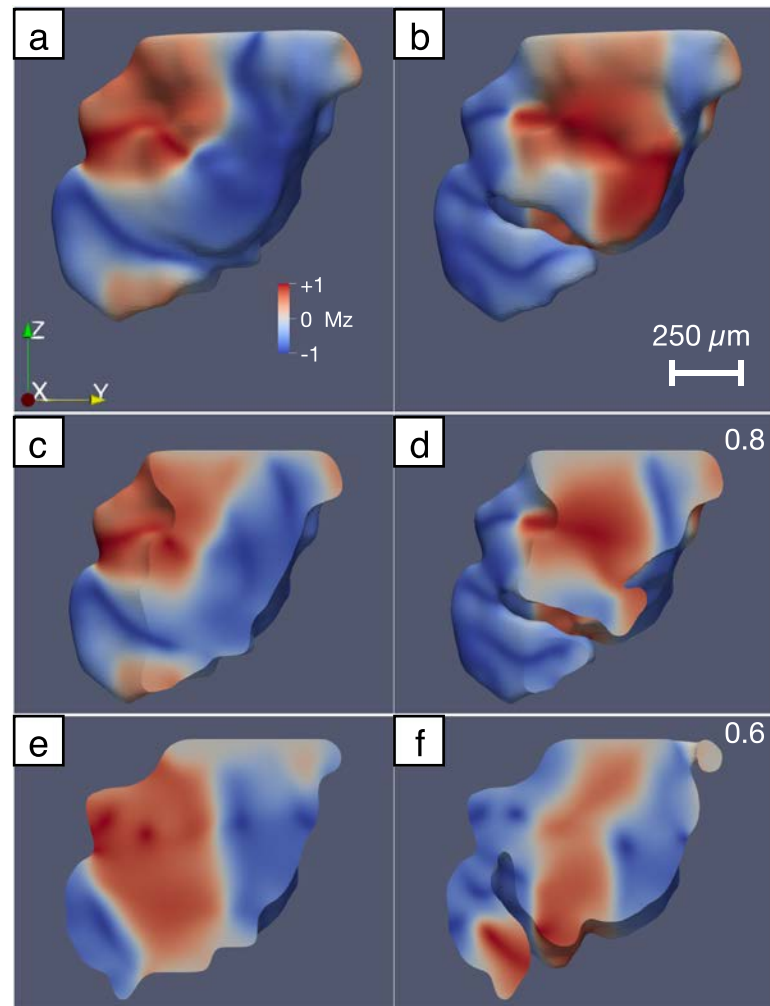
Figure 5. Modeling results of grains G4N (left) and G4W (right). Color shading represents the z component of magnetization from -1 (blue) to $+1$ (red). (a, b) Surface magnetization on the mesh geometries. Cross sections at $x = 800$ nm (c, d) and $x = 600$ nm (e, f) through the mesh show the internal magnetization structures with relatively sharp domain-like areas separated by domain wall-like rapid magnetization changes.

supporting information Figure S3 for remanence states in the other applied field directions). The color indicates deviation of the magnetization from the z direction, where red is aligned with the positive z direction and blue is aligned with the negative z direction. Figures 5c–5f show cross sections through the model to show the internal magnetization structures within the mesh. G4W has a more complex magnetization structure with smaller regions of uniform magnetization than G4N.

In Figure 6 the vorticity, anisotropy energy and exchange energy is shown for grains G4N and G4W. In both grains the anisotropy energy is broadly distributed (Figures 6c and 6d), such that no clearly developed domain walls with focused anisotropy energy peaks are observed. The exchange energy is lower in approximately the same areas where anisotropy energy is higher (Figures 6e and 6f). In both cases these regions also correspond to those where the vorticity is largest (Figures 6a and 6b). Together, these structural features represent a transition state between simple vortex states with swirl-like flux closure and classical multido-main structures (Landau & Lifschitz, 1935).

The results of the simulated hysteresis loops of particles G4N and G4W (Figure 7a) and particles G5N and G5W (Figure 7b) show substantial directional variation, although all coercivities are relatively small (Table 1 for G4N and G4W and supporting information Table S1 for G5N and G5W). The directional averages of the loops are given by black lines (solid or dashed in Figure 7). These essentially represent an
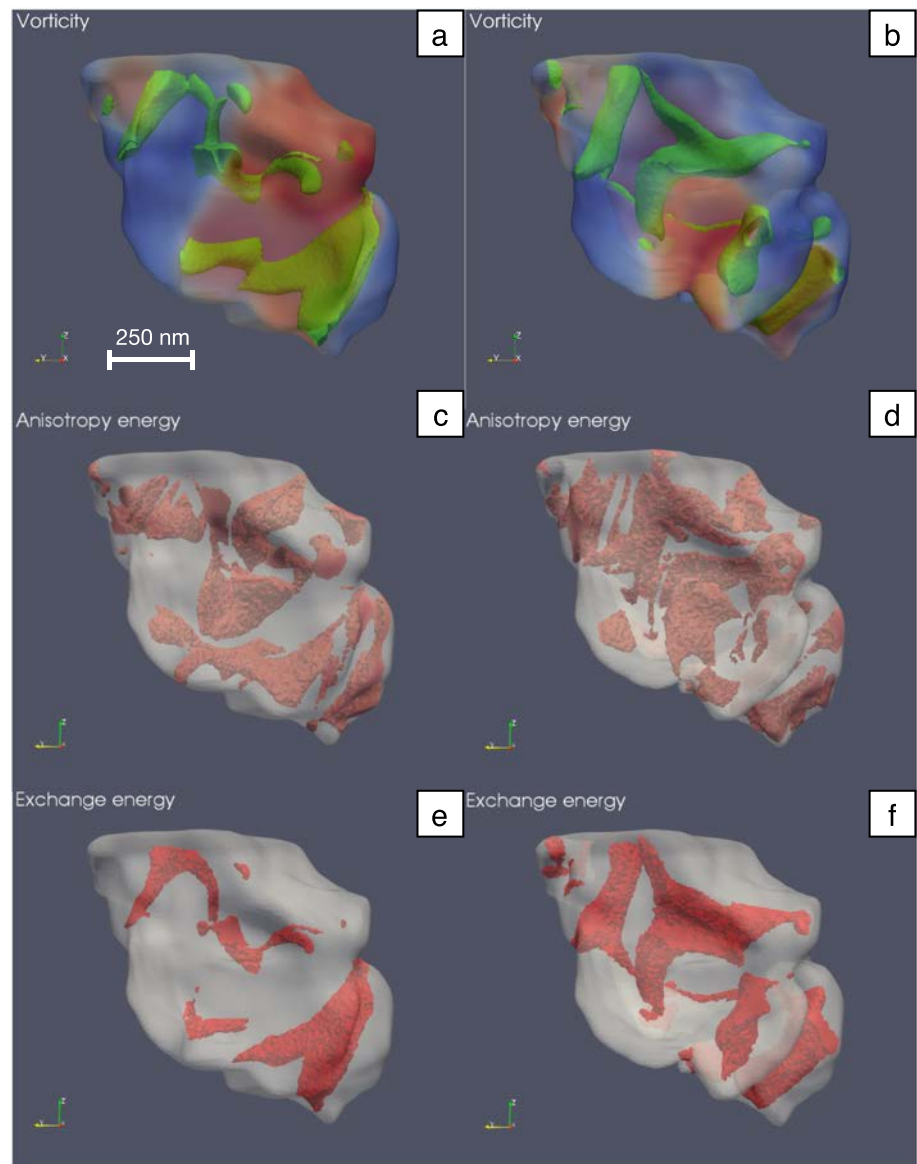
Figure 6. Modeling results of grain G4N, without microstructures (left), and G4W, with exsolution microstructures (right). The grain is rotated by 180° with respect to Figure 5. Color shading represents the z component of the magnetization from −1 (blue) to +1 (red). (a, b) Surface magnetization on the mesh geometries. The green 20% isosurfaces delineate regions of elevated vorticity of the moment vector field. (c and d) Anisotropy energy: the red surfaces indicate anisotropy energies above a local threshold of 30–33% and thus correspond to potential domain wall locations. (e and f) Red isosurfaces delineate regions of exchange energy densities below 7% of the maximum value and thus minimal magnetization change. They therefore indicate possible magnetic domains.

ensemble of similar but randomly oriented particles in the bulk sample. The insets in Figures 7a and 7b provide enlarged views near the origin to resolve better the variability of H_c and M_{rs}. Rescaled versions of the average loops are separately plotted in Figure 7c.

4. Discussion

With lengths of ~600 nm and widths of ~400 nm both simulated particles are larger than SD magnetite grains. Their magnetization structures contain multiple vortex structures linked to emerging separation of
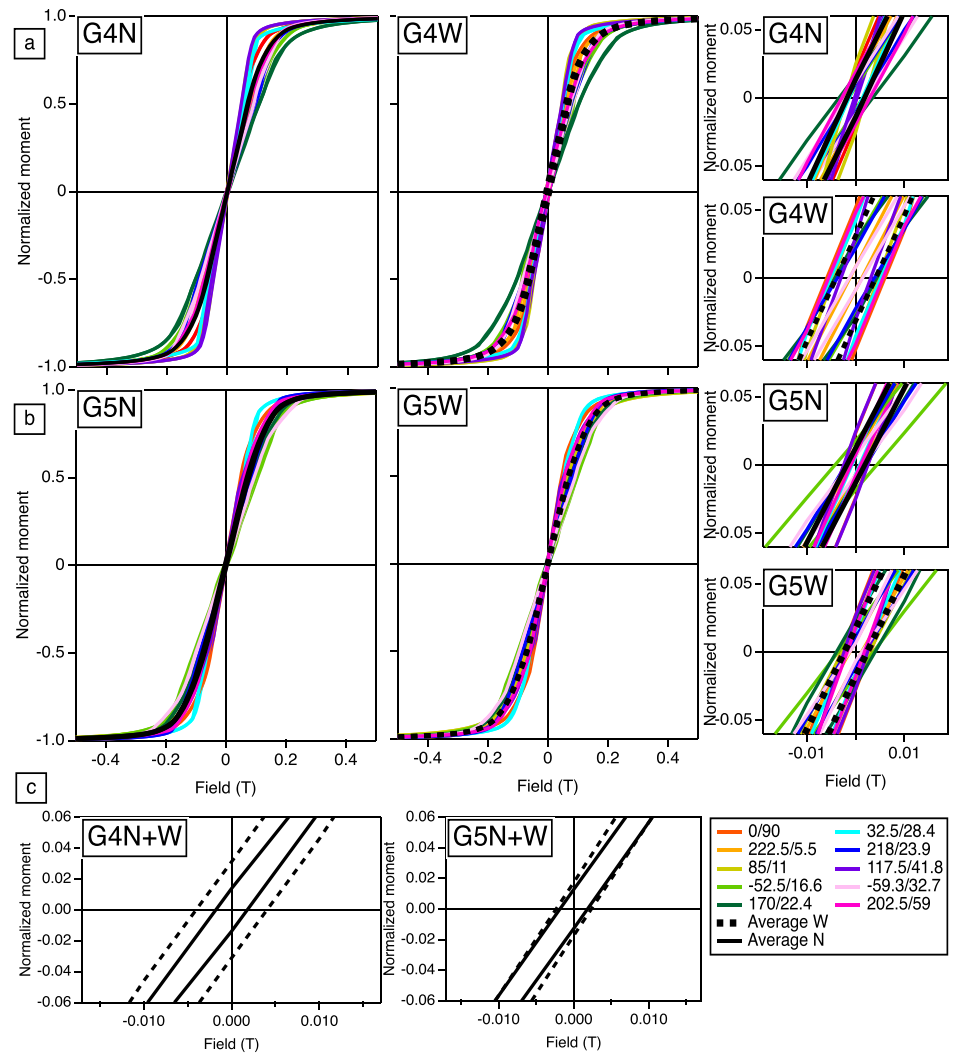
Figure 7. Modeled hysteresis loops for (a) particles G4N and G4W and (b) particles G5N and G5W. For each of the particles 10 hysteresis loops were obtained corresponding in 10 external field directions. The black solid lines show the averages of the 10 hysteresis loops for the models G4N and G5N, which do not contain oxidation-exsolution lamellae, and the black dashed lines show the average hysteresis loops for G4W and G5W, which do contain exsolution lamellae. On the right the area around the origin in shown at higher magnification. For clarification, (c) shows the area around the origin for the average loops of G4N and G4W on one plot, and for G5N and G5W on another plot.

domains by domain walls. That multiple vortex cores are present is also confirmed by the vorticity of the moment vector field.

In Figure 8 the squareness M_{rs}/M_s is plotted against the coercivity H_c for the modeled hysteresis loops of particles G4N and G4W. As a reference, the solid line represents low-Ti magnetite, the dashed line TM60 (Wang & Van der Voo, 2004), and the dotted line magnetite (Hodych, 1996). Green symbols mark the mean values for particles G4N (circles) and G4W (diamonds). We interpret that the higher mean values in G4W are due to the oxidation-exsolution microstructures in the grain. However, these values are still much lower than the measured bulk sample results, which are in the direction indicated by the arrow. The data points are colored according to the angle φ between the applied field direction, and the longest axis of the modeled particle from blue (φ = 0, aligned) to red (φ = π/2, orthogonal). The data points for models where the external field direction is aligned better with the direction of maximal particle elongation fall below the lines for magnetite and low-Ti magnetite, whereas the less aligned models plot closer to these lines.
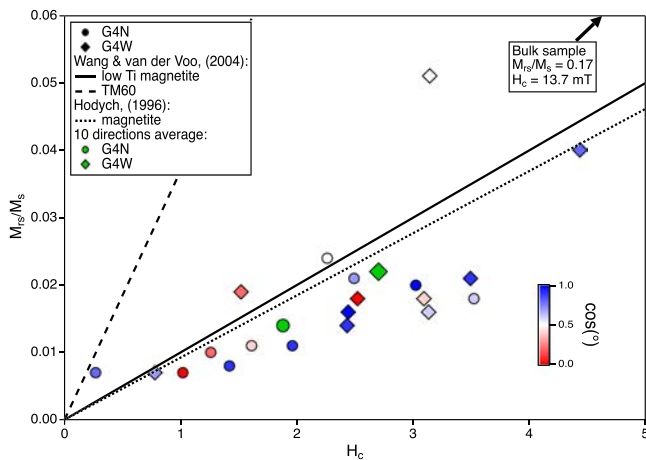
Figure 8. Squareness-coercivity plot for the hysteresis parameters from particles G4N (circles) and G4W (diamonds). The dashed line indicates TM60 data, and the solid line low-Ti magnetite, as described by Wang and Van der Voo (2004). The dotted line is for magnetite as calculated by Hodych (1996, and references therein). The samples are colored by the cosine of the angle of the applied field with respect to the longest axis of the particle. Blue indicates the field direction is aligned with the long axis of the particle, and red indicates the field direction is perpendicular to the long axis of the particle. In blue the mean squareness and mean coercivity from the 10 modeled directions of G4N and G4W are given.

Hodych (1990) reports that saturation remanence and coercivity in multidomain magnetite are primarily controlled by internal stress opposing domain wall motion. The self-demagnetizing factor N in multidomain grains is approximately related to saturation remanence and coercivity by $N = H_c/M_{rs}$ (Hodych, 1996; Néel, 1955). Here the calculated self-demagnetizing factors from the average of the modeled loops are $N = 0.24$ for G4N, and $N = 0.21$ for G4W. There is a slightly lower value for the grain with oxidation-exsolution lamellae (G4W). The slopes of both of the averaged hysteresis loops are steeper than the slope for an ideal nearly spherical particle, which is expected to have $N \sim 1/3$. This suggests that the magnetization structures are influenced by deviations from the ideal 3-D geometry, leading to an increased average coercivity.

The self-demagnetizing factor can be calculated for each modeled loop of the particles. The individual values of N are listed in Table 1 for G4W and G4N and in supporting information Table S1 for G5W and G5N.

The micromagnetic modeling results confirm that shape modification by oxidation-exsolution microstructures affects the magnetization (Figures 9a and 9b). The hysteresis parameters H_c and M_{rs} increase in the particles with lamellae. For example, the coercivity of grain G4N is 1.5 times higher, and the squareness ratio twice as high, as in grain G4W. However, the modeled hysteresis parameters are still a factor of 10 lower than those of the experimental hysteresis loops on Sample ST63.

The difference between the modeled and experimental hysteresis loops is not limited to increased coercivity values. The slow approach to saturation of the measured loops indicates the presence of a strong additional anisotropy energy that is counteracting the field alignment of the magnetization. The most likely sources of such an additional anisotropy are internal stresses in the grain.

To quantify the average amount of internal stress, we estimate the reversible work (U_{rev}) that is performed against stress during the approach to saturation. The difference in U_{rev} between the modeled and the measured bulk hysteresis loops (Figure 9c) can then be related to the internal stress σ via $U_{rev} = \frac{4}{3} \times \lambda_s \times \sigma$ (Appel, 1987). Here the dimensionless isotropic magnetostriction constant for magnetite is $\lambda_s = 40 \times 10^{-6}$. The upper hysteresis branch of the modeled loop lies above the measured curve between 85 mT and saturation at around 600 mT (Figure 9c). The area between the curves in this range is $U_{rev} = 4,860$ J/m^3. From the above equation we find a stress $\sigma = 91$ MPa, which is higher than the average of 48 MPa found by Appel (1987) for Ti-rich titanomagnetite, but lower than the stress estimates of >200 MPa for some mid-ocean ridge basalts (Fabian, 2006).

Currently, a full micromagnetic model including realistic stress fields is not available. The problematic part is not to implement internal stress energy in MERRILL but rather to provide a realistic geometry of the internal stress field. As a simple approximation, internal stress can be simulated by modeling the same particles with variable uniaxial anisotropy, for example by using uniaxial anisotropy constants between $K = 20$ kJ/m^3 and $K = 50$ kJ/m^3, instead of the cubic anisotropy of magnetite with $K_1 = -13$ kJ/m^3. A model with $K = 30$ kJ/m^3 resulted in an upper hysteresis curve which indeed showed higher coercivity but still faster approach-to-saturation. Similar to the model result of Fabian (2006), a wider spread of K values appears necessary to model the measured curve.

The hysteresis parameters of the Stardalur lava samples are changed by the geometric effect of the oxidation-exsolution lamellae toward those of smaller particles. However, the differences between measured and modeled data cannot be explained only by size reduction. The effect of internal stress and interfaces appears to be of greater importance. The incorporation of realistic internal stress fields into MERRILL, and investigating their influence on the resulting hysteresis loops remains a challenge for future studies.
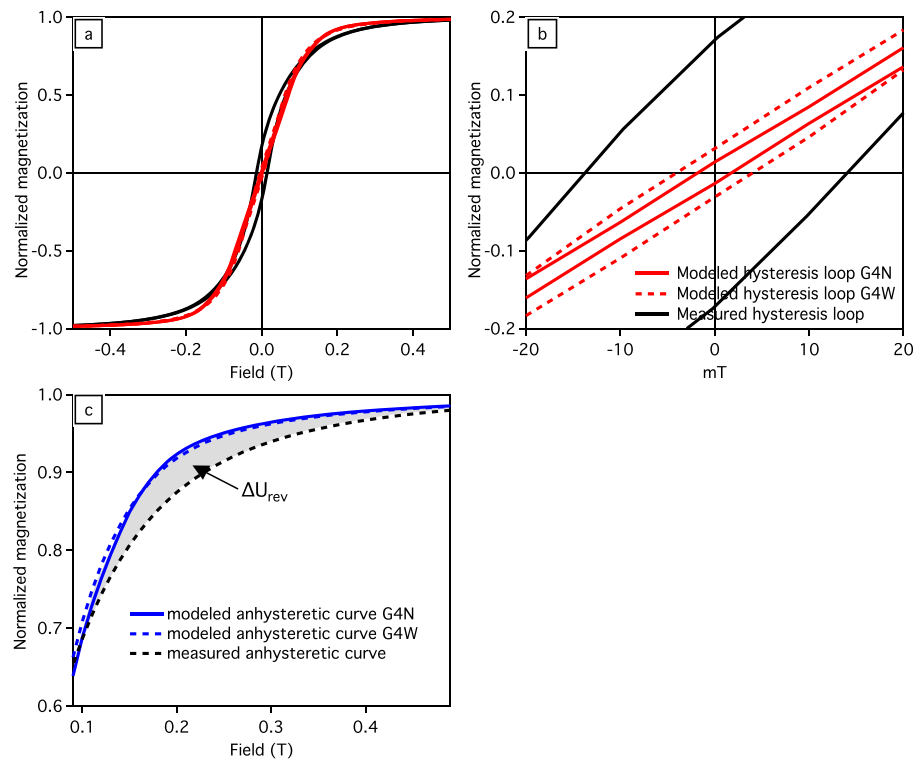
Figure 9. (a) Comparison of the measured hysteresis loop of ST63 with the modeled hysteresis loop. (b) Enlargement of the area around the origin. The coercivity is ~1.5 times smaller for the modeled loop without oxidation-exsolution lamellae than for the modeled loop with lamellae, and the M_{rs} is twice as high for the particle with microstructures (G4W) versus the particle without (G4N). However, measured loop for Sample ST63 has nearly 10 times higher coercivity and M_{rs} values compared to the models. (c) Comparison of the modeled and measured anhysteretic curves, obtained by averaging the upper and lower branch of the hysteresis loop. The approach-to-saturation is different for the modeled and measured data (ST63). The shaded area between the two curves in (c) between 0.1 and 0.5 T is the difference in reversible work (U_{rev}; Appel, 1987) between the two loops, which is used to calculate the difference in internal stress in both the measured and modeled samples.

5. Conclusions

- Basalt samples from Stardalur have unusually high NRM and Q values, and magnetomineralogical studies indicate predominance of magnetite. Another unusual property of these samples is the high abundance of oxidation-exsolution lamellae and spinel microstructures. Here we studied how these two observations are connected.
- Realistic geometries of oxy-exsolved magnetite, obtained by FIB-SEM nanotomography, were used in micromagnetic simulations by MERRILL to examine the influence of particle shape, size, and oxidation-exsolution lamellae on the magnetic properties of single particles. The same particles were modeled with and without lamellae.
- The models did not include stress anisotropy and therefore provide a calibration data set for the purely geometric enhancement of remanence due to widespread microstructures. Comparison between modeled and measured hysteresis properties was then used to assess the importance and quantity of internal stress in the exsolved particles.
- Stress-free models of grains with microstructures have up to 2 times higher M_{rs}/M_s ratio and a up to 1.5 times higher coercivity than the modeled grains without lamellae.
- Because the modeled coercivities are still a factor of 10 smaller than those measured in the bulk rock sample (ST63), this strongly suggests that internal stress from the oxidation-exsolution lamellae is the dominant mechanism of coercivity and remanence enhancement.
- The increase of anisotropy energy by stress can be estimated by comparing the approach-to-saturation behavior of the anhysteretic curves of models and measurements. Models of magnetite particles with

uniaxial stress anisotropy constant of $K = 30$ kJ/m may provide similar approach-to-saturation behavior as the measured curve.

- These results indicate that internal stress due to the formation of ilmenite lamellae dominates the acquisition and retention properties of NRM in rocks from the Stardalur basalts and results in a large remanent dominated magnetic anomaly of 27,000 nT above background.

References

Ahrens, J., Geveci, B., & Law, C. (2005). ParaView: An end-user tool for large-data visualization. *Visualization Handbook*, *836*, 717–731.

Akulov, N. (1931). Über den Verlauf der Magnetisierungskurve in starken Feldern. *Zeitschrift Für Physik*, *69*(11-12), 822–831. https://doi.org/10.1007/BF01339465

Almeida, T. P., Kasama, T., Muxworthy, A. R., Williams, W., Nagy, L., & Dunin-Borkowski, R. E. (2014a). Observing thermomagnetic stability of nonideal magnetite particles: Good paleomagnetic recorders? *Geophysical Research Letters*, *41*, 7041–7047. http://doi.org/10.1002/2014GL061432

Almeida, T. P., Kasama, T., Muxworthy, A. R., Williams, W., Nagy, L., Hansen, T. W., et al. (2014b). Visualized effect of oxidation on magnetic recording fidelity in pseudo-single-domain magnetite particles. *Nature Communications*, *5*(1), B12S15. http://doi.org/10.1038/ncomms6154

Almeida, T. P., Muxworthy, A. R., Kovacs, A., Williams, W., Brown, P. D., & Dunin-Borkowski, R. E. (2016). Direct visualization of the thermomagnetic behavior of pseudo-single-domain magnetite particles. *Science Advances*, *2*(4), e1501801. http://doi.org/10.1126/sciadv.1501801

Appel, E. (1987). Stress anisotropy in Ti-rich titanomagnetites. *Physics of the Earth and Planetary Interiors*, *46*(1-3), 233–240. http://doi.org/10.1016/0031-9201(87)90185-3

Church, N. S., Fabian, K., & McEnroe, S. A. (2016). Nonlinear Preisach maps: Detecting and characterizing separate remanent magnetic fractions in complex natural samples. *Journal of Geophysical Research: Solid Earth*, *121*, 8373–8395. http://doi.org/10.1002/2016JB013465

Clark, D. A. (2014). Methods for determining remanent and total magnetisations of magnetic sources—A review. *Exploration Geophysics*, *45*(4), 271–304. http://doi.org/10.1071/EG14013

Day, R., Fuller, M., & Schmidt, V. A. (1977). Hysteresis Properties of Titanomagnetites - Grain-Size and Compositional Dependence. *Physics of the Earth and Planetary Interiors*, *13*(4), 260–267. http://doi.org/10.1016/0031-9201(77)90108-X

Dunlop, D. J. (2002). Theory and application of the Day plot (M_{rs}/M_s versus H_{cr}/H_c) 1. Theoretical curves and tests using titanomagnetite data. *Journal of Geophysical Research*, *107*(B3), 2056. http://doi.org/10.1029/2001JB000486

Egli, R. (2013). VARIFORC: An optimized protocol for calculating non-regular first-order reversal curve (FORC) diagrams. *Global and Planetary Change*, *110*, 302–320. http://doi.org/10.1016/j.gloplacha.2013.08.003

Einsle, J. F., Harrison, R. J., Kasama, T., Conbhuí, P. Ó., Fabian, K., Williams, W., et al. (2016). Multi-scale three-dimensional characterization of iron particles in dusty olivine: Implications for paleomagnetism of chondritic meteorites. *American Mineralogist*, *101*(9), 2070–2084. http://doi.org/10.2138/am-2016-5738CCBY

Evans, M. E., Krása, D., Williams, W., & Winklhofer, M. (2006). Magnetostatic interactions in a natural magnetite-ulvöspinel system. *Journal of Geophysical Research*, *111*, B12S16. http://doi.org/10.1029/2006JB004454

Evans, M. E., & Wayman, M. L. (1974). An investigation of the role of ultra-fine titanomagnetite intergrowths in palaeomagnetism. *Geophysical Journal of the Royal Astronomical Society*, *36*(1), 1–10. http://doi.org/10.1111/j.1365-246X.1974.tb03621.x

Fabian, K. (2006). Approach to saturation analysis of hysteresis measurements in rock magnetism and evidence for stress dominated magnetic anisotropy in young mid-ocean ridge basalt. *Physics of the Earth and Planetary Interiors*, *154*(3-4), 299–307. http://doi.org/10.1016/j.pepi.2005.06.016

Fabian, K., Kirchner, A., Williams, W., Heider, F., Leibl, T., & Hubert, A. (1996). Three-dimensional micromagnetic calculations for magnetite using FFT. *Geophysical Journal International*, *124*, 89–104.

Fabian, K., & Shcherbakov, V. P. (2018). Energy barriers in three-dimensional micromagnetic models and the physics of thermoviscous magnetization. *Geophysical Journal International*, *215*(1), 314–324.

Fang, Q., & Boas, D. A. (2009). Tetrahedral mesh generation from volumetric binary and grayscale images. In From nano to macro 2009 IEEE International Symposium on Biomedical Imaging (pp. 1142–1145). https://doi.org/10.1109/ISBI.2009.5193259

Friðleifsson, I. B., & Kristjánsson, L. (1972). The Stardalur magnetic anomaly, SW-Iceland. *Jökull*, *22*, 69–78.

Fukuma, K., & Dunlop, D. J. (2006). Three-dimensional micromagnetic modeling of randomly oriented magnetite grains (0.03–0.3 μm). *Journal of Geophysical Research*, *111*, B12S11. http://doi.org/10.1029/2006JB004562

Harrison, R. J., & Feinberg, J. M. (2008). FORCinel: An improved algorithm for calculating first-order reversal curve distributions using locally weighted regression smoothing. *Geochemistry, Geophysics, Geosystems*, *9*, Q05016. https://doi.org/10.1029/2008GC001987

Heisenberg, W. (1928). Zur Theorie des Ferromagnetismus. *Zeitschrift für Physik*, *49*, 619–636.

Helgason, Ö., Steinthorsson, S., Madsen, M. B., & Morup, S. (1990). On anomalously magnetic basalt lavas from Stardalur, Iceland. *Hyperfine Interactions*, *57*(1-4), 2209–2214. http://doi.org/10.1007/BF02405787

Hodych, J. P. (1990). Magnetic hysteresis as a function of low temperature in rocks: evidence for internal stress control of remanence in multi-domain and pseudo-single-domain magnetite. *Physics of the Earth and Planetary Interiors*, *64*(1), 21–36. http://doi.org/10.1016/0031-9201(90)90003-G

Hodych, J. (1996). Inferring domain state from magnetic hysteresis in high coercivity dolerites bearing magnetite with ilmenite lamellae. *Earth and Planetary Science Letters*, *142*(3-4), 523–533. http://doi.org/10.1016/0012-821X(96)00107-0

Khakhalova, E., & Moskowitz, B. M. (2019). High-Temperature Observation of Transdomain Transitions in Vortex States in Intermediate Titanomagnetite. *Journal of Geophysical Research-Solid Earth*, *142*(2), 478–12. http://doi.org/10.1029/2019JB017857

Khakhalova, E., Moskowitz, B. M., Williams, W., Biedermann, A. R., & Solheid, P. (2018). Magnetic vortex states in small octahedral particles of intermediate titanomagnetite. *Geochemistry, Geophysics, Geosystems*, *41*, 717–713. http://doi.org/10.1029/2018GC007723

Kittel, C. (1949). Physical theory of ferromagnetic domains. *Reviews of Modern Physics*, *21*(4), 541–583. http://doi.org/10.1103/RevModPhys.21.541

Kristjánsson, L. (2002). Estimating properties of the paleomagnetic field from Icelandic lavas. *Physics and Chemistry of the Earth*, *27*(25-31), 1205–1213. http://doi.org/10.1016/S1474-7065(02)00122-5

Kristjánsson, L. (2013). The Stardalur magnetic anomaly, SW-Iceland: Aa review of research in 1968–2012. *Jökull*, 1–16.

Landau, L.D., Lifshitz, E., 1935. On the theory of the dispersion of magnetic perme-ability in ferromagnetic bodies. *Phys. Z. Sowjetunion*, *8* (153), 101–114.

Larson, E., Ozima, M., Ozima, M., Nagata, T., & Strangway, D. (1969). Stability of remanent magnetization of igneous rocks. *Geophysical Journal of the Royal Astronomical Society*, *17*(3), 263–292. http://doi.org/10.1111/j.1365-246X.1969.tb00237.x

Lascu, I., Einsle, J. F., Ball, M. R., & Harrison, R. J. (2018). The vortex state in geologic materials: A micromagnetic perspective. *Journal of Geophysical Research: Solid Earth*, *2*, 717–7304. http://doi.org/10.1029/2018JB015909

Muxworthy, A. (2003). Effect of magnetostatic interactions on the hysteresis parameters of single-domain and pseudo-single-domain grains. *Journal of Geophysical Research*, *108*(B11), 2517. http://doi.org/10.1029/2003JB002588

Nagy, L., Williams, W., Muxworthy, A. R., Fabian, K., Almeida, T. P., Conbhuí, P. Ó., & Shcherbakov, V. P. (2017). Stability of equidimensional pseudo-single-domain magnetite over billion-year timescales. *Proceedings of the National Academy of Sciences*, *114*(39), 10,356–10,360. http://doi.org/10.1073/pnas.1708344114

Nagy, L., Williams, W., Tauxe, L., & Muxworthy, A. R. (2019a). From nano to micro: Evolution of magnetic domain structures in multi-domain magnetite. *Geochemistry, Geophysics, Geosystems*, *20*, 2907–2918. http://doi.org/10.1029/2019GC008319

Nagy, L., Williams, W., Tauxe, L., Muxworthy, A. R., & Ferreira, I. (2019b). Thermomagnetic recording fidelity of nanometer-sized iron and implications for planetary magnetism. *Proceedings of the National Academy of Sciences of the United States of America*, *116*(6), 1984–1991. PMID: 30670651

Néel, L. (1955). Some theoretical aspects of rock-magnetism. *Advances in Physics*, *4*(14), 191–243. http://doi.org/10.1080/00018735500101204

Newell, A. J., & Merrill, R. T. (1999). Single-domain critical sizes for coercivity and remanence. *Journal of Geophysical Research-Solid Earth*, *104*(B1), 617–628. http://doi.org/10.1029/1998JB900039

Nichols, C. I. O., Einsle, J. F., Im, M. Y., Kasama, T., Saghi, Z., Midgley, P. A., & Harrison, R. J. (2019). Field response of magnetic vortices in dusty olivine from the Semarkona Chondrite. *Geochemistry, Geophysics, Geosystems*, *20*, 1441–1453. http://doi.org/10.1029/2018GC008159

Ó'Conbhuí, P., Williams, W., Fabian, K., Ridley, P., Nagy, L., & Muxworthy, A. R. (2018). MERRILL: Micromagnetic Earth related robust interpreted language laboratory. *Geochemistry, Geophysics, Geosystems*, *43*, 8426–8427. http://doi.org/10.1002/2017GC007279

Pike, C. R. (2003). First-order reversal-curve diagrams and reversible magnetization. *Physical Review B*, *68*(10), 104424. http://doi.org/10.1103/PhysRevB.68.104424

Pike, C. R., Roberts, A. P., & Verosub, K. L. (1999). Characterizing interactions in fine magnetic particle systems using first order reversal curves. *Journal of Applied Physics*, *85*(9), 6660–6667. http://doi.org/10.1063/1.370176

Roberts, A. P., Pike, C. R., & Verosub, K. L. (2000). First-order reversal curve diagrams: A new tool for characterizing the magnetic properties of natural samples. *Journal of Geophysical Research*, *105*(B12), 28,461–28,475.

Shaar, R., & Feinberg, J. M. (2013). Rock magnetic properties of dendrites: Insights from MFM imaging and implications for paleomagnetic studies. *Geochemistry, Geophysics, Geosystems*, *14*, 407–421. http://doi.org/10.1002/ggge.20053

Shah, J., Williams, W., Almeida, T. P., Nagy, L., Muxworthy, A. R., Kovács, A., et al. (2018). The oldest magnetic record in our solar system identified using nanometric imaging and numerical modeling. *Nature Communications*, *9*(1), 1173–1176. http://doi.org/10.1038/s41467-018-03613-1

Stange, M. (2016) The magnetic and mineralogical properties of the Stardalur Volcano, Iceland. (MSc thesis). Norwegian University of Science and Technology.

Vahle, C., Kontny, A., Gunnlaugsson, H. P., & Kristjánsson, L. (2007). The Stardalur magnetic anomaly revisited—New insights into a complex cooling and alteration history. *Physics of the Earth and Planetary Interiors*, *164*(3-4), 119–141. http://doi.org/10.1016/j.pepi.2007.06.004

Wang, D., & Van der Voo, R. (2004). The hysteresis properties of multidomain magnetite and titanomagnetite/titanomaghemite in mid-ocean ridge basalts. *Earth and Planetary Science Letters*, *220*(1-2), 175–184. http://doi.org/10.1016/S0012-821X(04)00052-4

Williams, W., & Dunlop, D. J. (1995). Simulation of magnetic hysteresis in pseudo-single-domain grains of magnetite. *Journal of Geophysical Research*, *100*(B3), 3859–3871. http://doi.org/10.1029/94JB02878

Witt, A., Fabian, K., & Bleil, U. (2005). Three-dimensional micromagnetic calculations for naturally shaped magnetite: Octahedra and magnetosomes. *Earth and Planetary Science Letters*, *233*(3-4), 311–324. http://doi.org/10.1016/j.epsl.2005.01.043

Yu, Y., & Tauxe, L. (2008). Micromagnetic models of the effect of particle shape on magnetic hysteresis. *Physics of the Earth and Planetary Interiors*, *169*(1-4), 92–99. http://doi.org/10.1016/j.pepi.2008.07.006